

Global survey of the immunomodulatory potential of common drugs

Gregory I Vladimer^{1,8} , Berend Snijder^{1,7,8} , Nikolaus Krall¹ , Johannes W Bigenzahn¹ , Kilian V M Huber^{1,2} , Charles-Hugues Lardeau^{1,3}, Kumar Sanjiv⁴, Anna Ringler^{1,3}, Ulrika Warpman Berglund⁴, Monika Sabler¹, Oscar Lopez de la Fuente¹, Paul Knöbl⁵, Stefan Kubicek^{1,3} , Thomas Helleday⁴, Ulrich Jäger⁵ & Giulio Superti-Furga^{1,6*} 

Small-molecule drugs may complement antibody-based therapies in an immune-oncology setting, yet systematic methods for the identification and characterization of the immunomodulatory properties of these entities are lacking. We surveyed the immunomodulatory potential of 1,402 small chemical molecules, as defined by their ability to alter the cell-cell interactions among peripheral mononuclear leukocytes *ex vivo*, using automated microscopy and population-wide single-cell image analysis. Unexpectedly, ~10% of the agents tested affected these cell-cell interactions differentially. The results accurately recapitulated known immunomodulatory drug classes and revealed several clinically approved drugs that unexpectedly harbor the ability to modulate the immune system, which could potentially contribute to their physiological mechanism of action. For instance, the kinase inhibitor crizotinib promoted T cell interactions with monocytes, as well as with cancer cells, through inhibition of the receptor tyrosine kinase MSTR1 and subsequent upregulation of the expression of major histocompatibility complex molecules. The approach offers an attractive platform for the personalized identification and characterization of immunomodulatory therapeutics.

High-content screening using automated fluorescence microscopy has allowed us to objectivize and quantify a great variety of cellular parameters, and it has provided an attractive platform to perform genetic or chemical perturbation screens at unprecedented accuracy and robustness due to the statistical power derived from the large number of events monitored. In particular, the approach has enabled the visualization of the influence of cell-cell and cell-microenvironment interactions, which contribute to population-level phenotypes¹. It has further facilitated the high-throughput screening of co-culture systems, identifying phenotypes of the individual subpopulations, as well as resolving the interplay between cell populations that may contribute to an integrated drug response.

Automated microscopy has not yet been adapted for the screening of non-adherent and adherent leukocytes present in blood as a model to study immunology, even as traditional microscopy has proven crucial to understanding the complex interaction dynamics of the immune system². Because other high-throughput screening technologies have been used to measure the effect of indirect factors on immune response propagation, such as signaling proteins and soluble cytokines, automated microscopy can be expected to provide the unique spatial resolution and throughput required to quantitatively screen the modulation of direct signaling by cell-cell contacts (receptor-mediated signaling) that drives an immune response. Such information on cell-cell contacts in blood for large drug libraries is of particular interest, as many successful drugs affect properties of cells that are not cell autonomous but rather rely on the modification of the relationship between cells; this is best illustrated by the recent success of cancer immunotherapy³.

Modulation of both the innate and adaptive immune systems is a highly successful strategy in the treatment of systemic diseases such as inflammatory disorders and cancer, for which the innovation of targeted biological or chemical agents is at the forefront. For instance, the immunomodulatory drug pomalidomide, which induces cytotoxic T cell and NK cell activity, and immune-checkpoint inhibitors, such as the monoclonal antibody ipilimumab (which is specific for the T cell-inhibitory receptor CTLA4)⁴, alter the balance of co-stimulatory and co-inhibitory signals that manage self-tolerance and regulate T cell responses⁵. In both of these examples, the drug mediates cellular interactions that result in the death of the target cancer cell, a concept that underlies many of the immunomodulatory drugs that have proven successful in treating a variety of malignant diseases⁴.

Here we describe a high-throughput image-based screening method and analysis algorithm that robustly quantifies the immunomodulatory potential of small molecules and other therapeutics by measuring the changes in the physical interaction of leukocytes. With this method, phenotypic drug screening can be expanded to help realize entities that harness the inherent ability of effector cells, within peripheral blood, to propagate signals and function through direct physical contact—a major goal of immunotherapy.

RESULTS

Systematic quantification of leukocyte cell-cell contacts

We designed a pipeline to directly assay biologicals and chemical agents for their immunomodulatory properties, by measuring changes in cell-cell contacts of peripheral blood mononuclear cells

¹CeMM Research Center for Molecular Medicine of the Austrian Academy of Sciences, Vienna, Austria. ²Structural Genomics Consortium, University of Oxford, Oxford, UK and Target Discovery Institute, University of Oxford, Oxford, UK. ³Christian Doppler Laboratory for Chemical Epigenetics and Anti-infectives, CeMM Research Center for Molecular Medicine of the Austrian Academy of Sciences, Vienna, Austria. ⁴Science for Life Laboratory, Division of Translational Medicine and Chemical Biology, Department of Medical Biochemistry and Biophysics, Karolinska Institutet, Stockholm, Sweden.

⁵Department of Internal Medicine I, Division of Hematology and Hemostaseology, Medical University of Vienna, Vienna, Austria. ⁶Center for Physiology and Pharmacology, Medical University of Vienna, Vienna, Austria. ⁷Present address: Department of Biology, Institute of Molecular Systems Biology, Zurich, Switzerland. ⁸These authors contributed equally to this work. *e-mail: gsuperti-furga@cemm.oew.ac.at

(PBMCs) *ex vivo* using population-wide single-cell microscopy of PBMC monolayers (Supplementary Results, Supplementary Fig. 1a and Online Methods). Individual cell types were identified using fluorescently tagged antibodies, in various non-overlapping combinations, specific for extracellular markers that are unique to the PBMC subpopulations of interest. This revealed extensive cell-cell interactions between the different subpopulations (Fig. 1a). Because the method requires only small amounts of material for each test, all of the assays can be performed in the blood of an individual donor, which reduces background inflammation due to human leukocyte antigen (HLA) mismatching. To assess whether the observed interactions among cells were functionally meaningful and to benchmark the assay, we made use of four biologicals that are known to decrease or increase selected cell-cell contacts: a major histocompatibility complex class II (MHC-II)-blocking antibody, two clinically used antibodies (rituximab and blinatumomab; Supplementary Fig. 1b) and lipopolysaccharide (LPS).

The interaction between T cells and professional antigen-presenting cells (APCs), including dendritic cells and macrophages, is an essential step in triggering an adaptive immune response. APCs present foreign antigens via MHC-II receptors to CD3 receptors on T cells (also known as T cell receptors; TCRs), which can lead to a targeted immune response⁶. Antibodies that recognize the extracellular portion of the MHC-II receptor are known to efficiently obstruct this interaction (Supplementary Fig. 1b, left). Indeed, when we stimulated PBMCs from a healthy individual with vesicular stomatitis virus (VSV) in the absence or presence of an MHC-II-specific blocking antibody, the percentage of CD11c⁺ dendritic cells that were in direct contact with CD3⁺ T cells was significantly reduced by the presence of the MHC-II-specific blocking antibody before infection, on average from 33% to 25% ($P < 0.028$; Fig. 1b) as measured over a total of 124,059 cell-cell contacts. Such interaction frequencies are, however, dependent on several variables that directly influence the outcome. In the scenario just described, they include: the fraction of all cells that are CD11c⁺ (x_a), the fraction of all cells that are CD3⁺ (x_b), and the total cell density or overall clustering index, which can be expressed as the fraction of all PBMCs that directly contact one or more PBMCs (x_i). Indeed, all three variables showed fluctuations in the MHC-II-specific blocking antibody experiment described in Figure 1b, among others, due to stimulus-dependent differences in cellular activation (Supplementary Fig. 1c)⁷, which need to be statistically accounted for when interpreting such interaction frequencies. The fraction of cells that are of type 'A' and that interact with cells of type 'B', assuming that cellular positions and relative abundance of subpopulations are kept equal but cellular identities are shuffled, is given by the formula $E = x_a \times x_b \times x_i$, where x_a is the fraction of cells of type A, x_b is the fraction of cells of type B, and x_i is the fraction of cells with one or more cell contacts. Bootstrap analysis confirmed the equation, consistent with the fact that the three variables function as independent probabilities in this context (Supplementary Fig. 1d). Scoring alterations in the interaction frequency relative to E then gives an internally normalized interaction frequency, which we have termed the 'interaction score'. Further information on the interaction score can be found in the Online Methods. The interaction score indicates how much the observed interaction frequency deviates from what would be expected by random chance occurrence, which makes it robust to alterations in the relative abundance of either subpopulation, as well as to alterations in overall cell density or in the number of cell-cell contacts. We have used arrows to indicate the directionality of the interaction score, i.e., relating to the fraction of type A cells that interact with type B cells, which can deviate from the fraction of type B cells that interact with type A cells, in the case of many-to-one cell-cell contacts. After correcting for these influences, we found that the MHC-II-specific blocking antibody not only reduced the CD11c⁺→CD3⁺ T cell interactions under the

VSV-stimulated conditions but that it also did so in the unstimulated state (Fig. 1c and Supplementary Fig. 1e), which is likely explained by reduced antigen 'scanning' by T cells^{8,9}. As expected, the presence of either an isotype IgG control antibody or a blocking antibody to CD54, which functions as a co-stimulatory signal and is typically not highly expressed on unstimulated monocytes¹⁰, did not significantly alter the CD11c⁺→CD3⁺ T cell interaction score in the unstimulated conditions (Supplementary Fig. 1f). Furthermore, contact-dependent immune activity was described as early as 1970, in which it was observed that clustering of CD14⁺ monocytes that were stimulated by bacterial lipopolysaccharides (LPS) is an activation-associated signal¹¹. Accordingly, the interaction score revealed a significant ($P < 0.05$) increase in the interaction between CD14⁺ monocytes after LPS treatment (Supplementary Fig. 1g). In these examples, immune activation and modulation can strongly drive cell proliferation, which could potentially affect the number of cells within the interacting subpopulations that are being measured. To additionally confirm that the interaction score was robust to either gain or loss of cellular subpopulations, we simulated fluctuations in the proportion of type A and type B cells over a wide range (5% to 95%) and then measured the interaction score of A↔B; synthetic data provided a controlled environment without compounding factors, such as background inflammation. As expected, we found that the score was inherently robust to modifications in cell number (Supplementary Fig. 2a), which enabled us to measure altered cell-cell contacts even in the context of cell proliferation and cell death.

The anticancer biologicals rituximab and blinatumomab induce NK cell-to-B cell-mediated killing (Supplementary Fig. 1b, middle) and T cell-to-B cell-mediated killing (Supplementary Fig. 1b, right), respectively, in which the function of the killing depends on direct physical contacts between effector and target cells¹²⁻¹⁴. Incubation with these biologicals resulted in not only a dose-dependent increase in the respective interaction scores but also in a concomitant loss of target cells (Fig. 1d,e and Supplementary Fig. 2b). In the case of blinatumomab, the results were independent of the marker that was used to identify the B cells as the target cell type (Fig. 1e). Even with the reduction in the population of the target B cells, the interaction score was still increased, due to the score's normalization to variations in subpopulation numbers (Fig. 1d,e), as described above. Thus, the recapitulation of the effects of biologicals with well-defined mechanisms of action, as measured by population-wide imaged-based screening and spatial analyses, validates this method for use in an immunomodulatory screening campaign.

Although biologicals have great precision and efficacy in their mode of action, it would be advantageous to identify small chemical entities with specific immunomodulatory properties that could be more easily handled and manufactured. To determine what classes of drugs, if any, have unknown immunomodulatory effects, we surveyed a collection of 1,402 existing drugs (approved, investigational or experimental; Supplementary Data Set 1 and Supplementary Table 1) to see whether one could compare their effects with those of drugs with known immunomodulatory properties, such as steroids and NSAIDs.

Chemical rewiring of the leukocytic interaction network

Leukocyte interactions across the 1,402 compounds were screened in quadruplicate, which resulted in the identification and analysis of the cell-to-cell contacts of over 80 million PBMCs from the blood of a single healthy donor in 7,680 wells. To induce a higher level of cell-cell contacts, alterations of PBMC cell-cell interactions were measured after immune stimulation with VSV, which induces an interferon (IFN)-based inflammatory immune response that is aimed at halting viral replication¹⁵. Pairwise combinations of four major PBMC subpopulations were stained after infection, using immunofluorescence. At the population-level, VSV infection, as measured

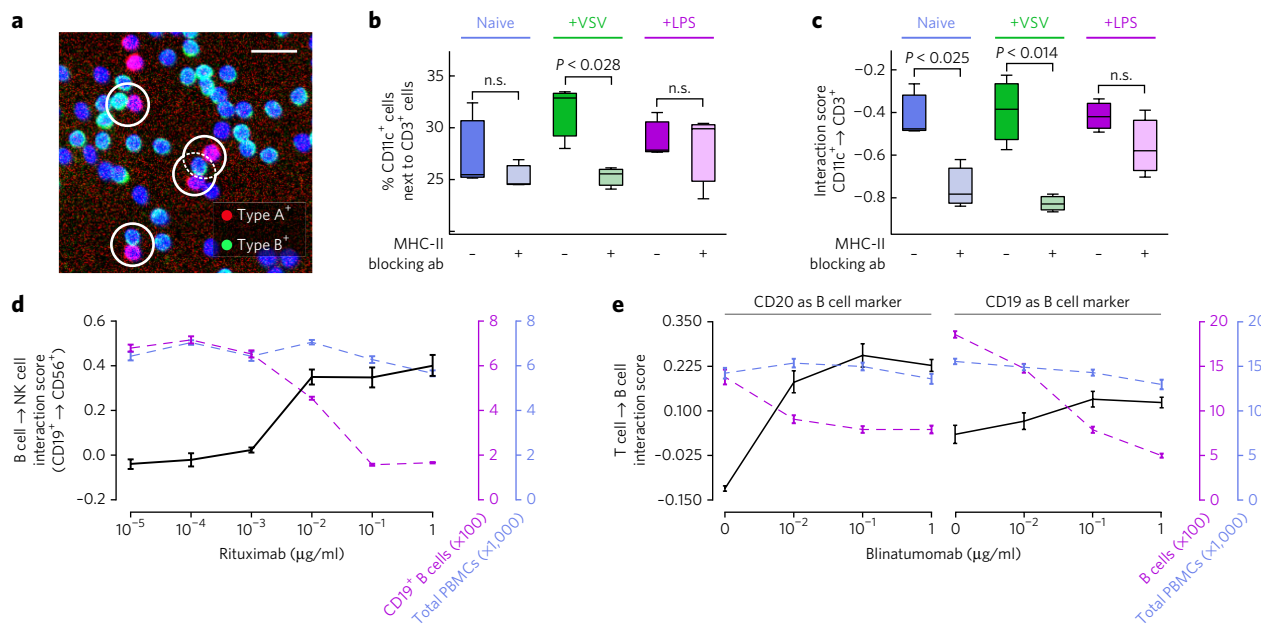


Figure 1 | Quantifying PBMC cell-cell interactions that are perturbed by biologicals. (a) Representative section of a $10\times$ image (of $n = 25,000$ images) from the high-throughput screening pipeline of cell-cell contacts between PBMC subpopulations, with selected contacts highlighted (white circles). Scale bar, $25\ \mu\text{m}$. (b) Percentage of CD11c^+ cells in contact with CD3^+ cells in the absence (naive) or presence of stimulation with VSV or LPS, with or without pre-incubation with an MHC-II-specific blocking antibody. (c) $\text{CD11c}^+ \rightarrow \text{CD3}^+$ interaction scores corresponding to (d). Interaction score is calculated as the observed percentage of type A cells in relation to type B cells \log_2 -relative to what is expected if the data were randomized. (d) The interaction score of CD19^+ B cells $\rightarrow \text{CD56}^+$ NK cells (black axis; left), CD19^+ B cell counts (purple axis; right), or total PBMC counts (blue axis; far right) as function of increasing rituximab concentration. (e) Interaction scores of (left plot) CD3^+ T cells $\rightarrow \text{CD19}^+$ B cells or (right plot) CD3^+ T cells $\rightarrow \text{CD20}^+$ B cells (black axis; left), B cell counts (purple axis; right), or total PBMC counts (blue axis; far right) as function of increasing blinatumomab concentration. Experiments in **b,c** were performed in triplicate and are representative of three independent experiments. Experiments in **d,e** were performed in five technical replicates and are representative of $n = 5$ (d) or $n = 2$ (e) experiments from two healthy donors. In **d,e**, data are mean \pm s.e.m. of technical repeats. In **b,c**, boxes denote 25th to 75th percentiles, and whiskers indicate the maximal data points present within $1.5 \times$ the interquartile range (IQR) from the top and bottom of the boxes of technical repeat values. *P* values in **b,c** were determined by a Student's *t*-test; n.s., not significant.

by a single-cell green fluorescent protein (GFP) reporter, displayed high reproducibility (Fig. 2a and Supplementary Fig. 3a), and VSV preferentially infected myeloid lineage cells (Supplementary Fig. 3b), as expected⁷. Eighty compounds were found to decrease VSV infection, whereas 22 increased it (below -2 or above 2 s.d., with $P < 0.05$; Fig. 2b and Supplementary Fig. 3c). Notably, several known anti-inflammatory compounds, including corticosteroids, led to increased VSV infection (Fig. 2b and Supplementary Fig. 3d), which may indicate a functional blockage in cellular signaling pathways that rely on soluble factors and, furthermore, that these pathways are active in our model¹⁶.

After analyzing all 246×10^6 cell-cell contacts measured in the screen, we observed that the monocyte-lineage cells had significantly higher numbers of direct neighbors than the lymphocyte-lineage cells (Fig. 2c). We evaluated the interaction scores between the distinct subpopulations and observed the highest scores among and between CD11c^+ and CD14^+ monocytes (Fig. 2d), and lower (yet higher than those by random chance occurrence) interaction scores between all measured monocyte-lymphocyte pairs. In contrast, interaction scores of around zero, on average, were observed between B cells and T cells, and from T cells to any of the other cell types, which was indicative of baseline cell-cell contact frequencies equal to those expected by random chance occurrence for T cells (Fig. 2d). Overall, many more compounds were found to alter only leukocyte cell-cell contacts (11.6%) than those altered by only virus infection (2.5%) at 2 s.d. (Fig. 2e). Similarity in the molecular regulation of cell-cell receptor-mediated contacts would be expected to lead to similarity in the drug-induced alterations of those cell-cell contacts. Indeed, comparison of the overall results revealed the

highest similarity in the modulation of cell-cell contacts among and with monocyte-lineage cells (Fig. 2f).

To analyze the chemical modulation across the entire library, drug annotation enrichments over all interaction scores were calculated and displayed by hierarchical clustering (Fig. 2g; the full list of compounds and their specific immune modulation phenotype is attached as a resource in Supplementary Data Set 2). Inspection of the enriched drug classes that altered PBMC cell-cell contacts revealed the presence of four groups, which comprised predominant classes of drugs known to modulate the immune system: (i) steroidal anti-inflammatory compounds, such as glucocorticoids, that bind to steroid hormone receptors (Fig. 2g, dark gray); (ii) nonsteroidal anti-inflammatory drugs (NSAIDs), including arachidonate 5-lipoxygenase, and cyclooxygenase inhibitors (Fig. 2g, gray); (iii) drugs acting on or mimicking the signaling of the sympathetic nervous system, including catecholamines, adrenaline, dopamine, and associated receptor agonists and antagonists (Fig. 2g, light gray); and (iv) a group containing compounds that either have been described to act on other systems or were previously unreported drug classes (Fig. 2g, yellow). Comparison of the top 140 drugs with the strongest changed interaction scores to the 140 drugs with the strongest cytotoxicity revealed an overlap of only 11 drugs (7%; Supplementary Fig. 3e), indicating that the cell-cell contact analysis did not have a bias toward drugs with strongly altered cell population sizes.

Treatment with steroidal anti-inflammatory compounds not only led to strong increased VSV infection, as expected by their mechanism of action, but it also showed significant enrichment for decreased CD14^+ cell interactions (Fig. 2g,h). Steroidal anti-inflammatories

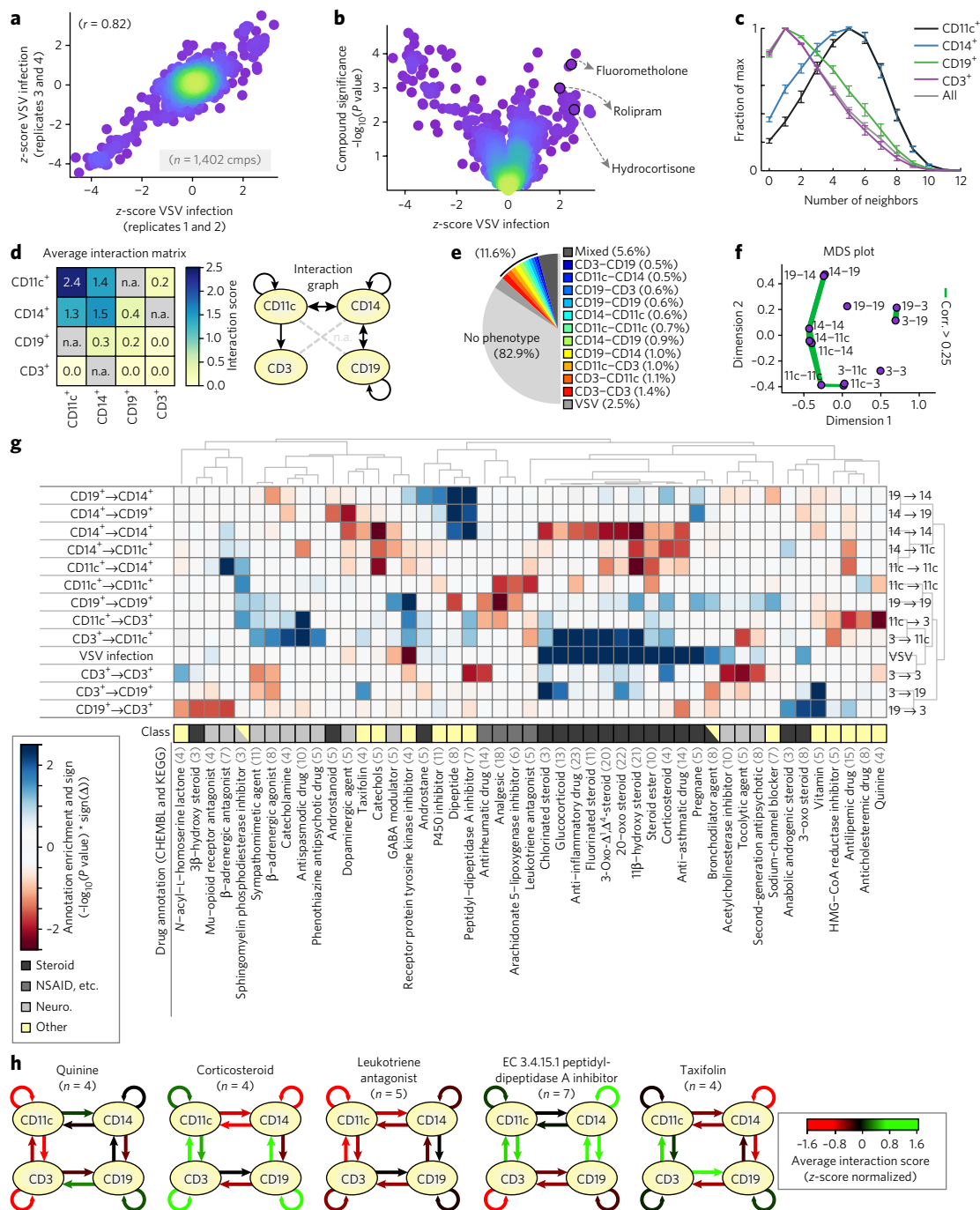


Figure 2 | Screening for chemical modifiers of PBMC cell-cell contacts. (a) Scatter plot showing reproducibility of VSV infection in four replicates (average of two replicates per axis). Dots correspond to compound, and color indicates data density. (b) Average change in VSV infection per compound (z-score-normalized) relative to the significance per compound ($-\log_{10}(P \text{ value})$). Selected anti-inflammatory compounds are indicated. (c) Distributions of the number of direct contacts (cell-cell neighbors) per cell type tracked, normalized to the maximum of each distribution; values were aggregated over all 1,402 drugs screened. Data are mean \pm s.e.m. (d) Left, interaction scores of each pairwise combination averaged over screen. n.a. (gray boxes), not measured. Right, visualization of the average interaction scores as an interaction graph. (e) Percentage of compounds with unique or mixed phenotypes at 2σ significance. (f) Multidimensional scaling plot of the similarity between results relative to each measured interaction. Green lines connect interactions whose screening results are ≥ 0.25 ; "Corr." indicates the Pearson's linear correlation coefficient. (g) Hierarchical clustering of the enrichment ($-\log_{10}(P \text{ value}) \times \text{sign}$ of the phenotype (either positive or negative interaction score)) for selected top-enriched drug classes over all of the interactions measured, including the VSV infection phenotype. Blue and red boxes indicate increased or decreased spatial phenotypes, respectively. Manual drug annotation class shown below. Light gray numbers in parentheses indicate number of compounds in that class. "Neuro." indicates the class of neuromodulating drugs. (h) Interaction graphs of the average phenotypes for selected annotations from g. Red and green arrows indicate decreased or increased average interaction scores (z-score-normalized), respectively; black arrows indicate no change. The data in a-h represent a large-scale screen performed in replicate or quadruplicate, at single-cell resolution (13,152 cells per well for 7,680 wells). Measurements in a,b were performed in quadruplicate. In c-f, summary statistics were combined for 1,402 compounds. The groups in g,h are represented by ≥ 3 compounds per annotation. The data in c-h represent 246,650,047 cell-cell interactions.

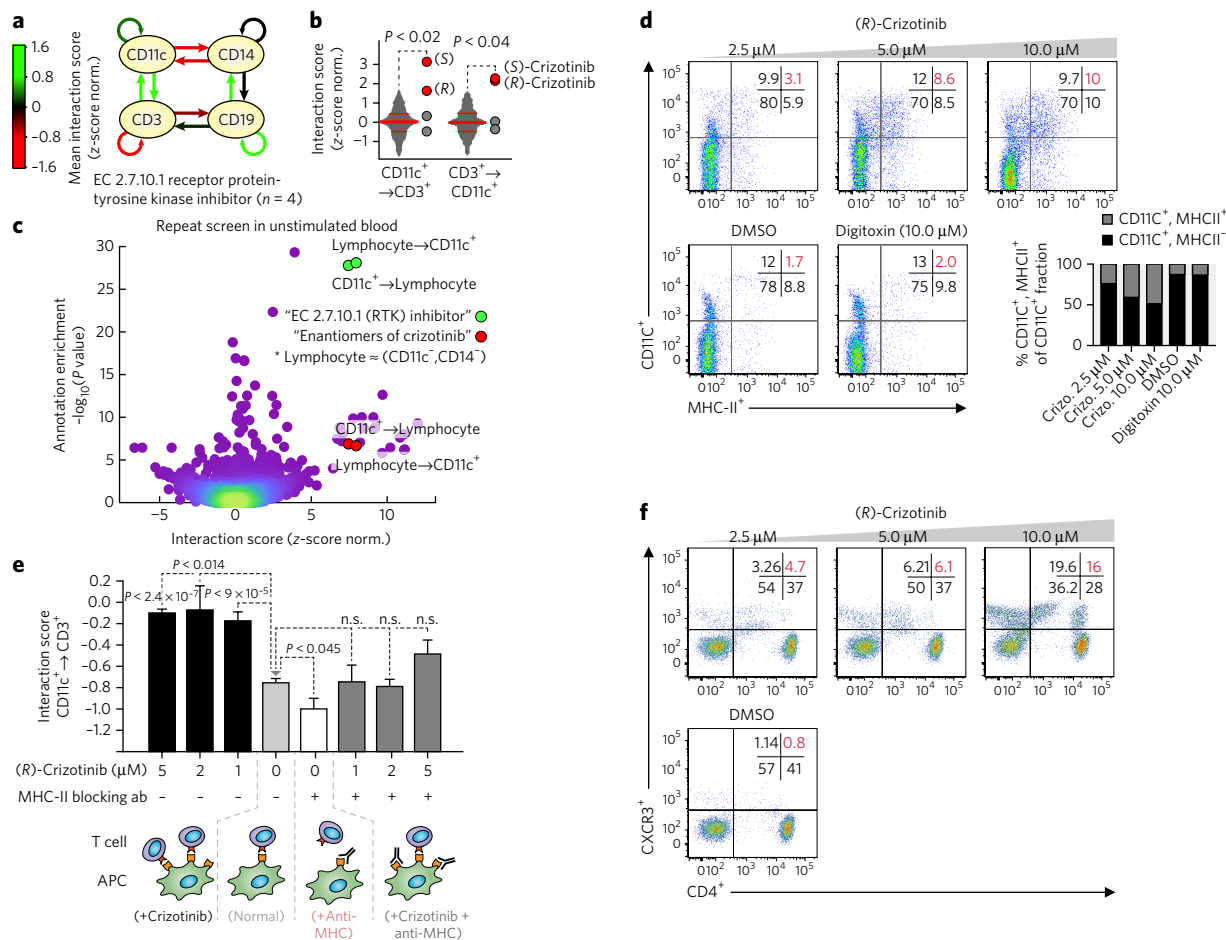


Figure 3 | Crizotinib increases T cell interactions with monocytes through upregulation of MHC-II. (a) Interaction graph of average interaction scores for compounds that are annotated as RTKis, using PBMCs from healthy donors; green and red arrows indicate increased and decreased interaction scores, respectively. (b) Interaction scores of CD11c⁺→CD3⁺ cells (left) and CD3⁺→CD11c⁺ cells (right) after treatment with (R)- and (S)-crizotinib (red dots), as compared to those for the other RTKis (gray dots), as well as the respective interaction score distributions over the entire screen (gray plots, with 25th, 50th and 75th percentiles indicated as horizontal lines). (c) Annotation enrichment analysis over all interaction scores measured in naive PBMCs. Dots indicate individual annotations and their cell-cell interactions. The y axis indicates significance of annotation enrichment for compounds with a certain phenotype. The x axis indicates the average z-score-normalized interaction score per annotation. Green dots indicate results for the RTKis and lymphocytes↔CD3⁺ interactions; red dots indicate the ‘enantiomers of crizotinib’ annotation and lymphocytes↔CD3⁺ interactions. (d) Flow cytometry analysis for MHC-II expression on CD11c⁺ cells of naive PBMCs after overnight incubation with (R)-crizotinib, digitoxin or DMSO. Bar graph (bottom right) represents percentage of double-positive (CD11c⁺MHCII⁺) cells in the CD11c⁺ fraction. (e) Top, interaction score of CD11c⁺→CD3⁺ cells after crizotinib treatment without (left) or with (right) a MHC-II-specific blocking antibody (n = 164,569 measured cell-cell interactions). Bottom, schematic of the interpretation of the results in the graphs. Significance values are relative to results observed with vehicle (DMSO) treatment only (0 μM (R)-crizotinib) and were determined by a t-test; n.s., not significant. (f) Flow cytometry analysis of CD4⁺ T cells that express the chemokine receptor CXCR3 (also known as CD183) (T_{H1} T cells) after overnight incubation with (R)-crizotinib. In a, b, data are from screens performed in quadruplicate; data in c are from screens performed in duplicate; data shown in d–f are representative of five (d) or three (e, f) repeats.

regulate the immune system via the glucocorticoid receptor and reduce the transcriptional activity of pro-inflammatory transcription factors, including NF-κB and IRF3 (ref. 17), which may explain the observed decreased clustering of CD14⁺ cells and increased amounts of VSV infection (Fig. 2g,h). CD14⁺ cell clustering was, in fact, the cell-cell interaction with the most significant correlation to VSV infection over all of the compounds measured (Supplementary Fig. 3f, left), with increased amounts of infection being associated with decreased clustering and vice versa ($P < 2.3 \times 10^{-5}$; Supplementary Fig. 3f, middle). The increased amount of CD14⁺ cell clustering observed after LPS stimulation (Supplementary Fig. 1g) combined with previous reports¹¹ singled out CD14⁺ cell clustering as the predominant spatial read-out of innate immune activation and suggested that some compounds reduced virus infection by activating an innate immune

reaction; these observations were further confirmed using PBMCs from a second healthy donor (Supplementary Fig. 3f, right).

In contrast to the effects seen with the steroidal anti-inflammatory compounds tested, we observed that several NSAIDs reduced CD11c⁺ cell clustering, CD19⁺ B cell clustering and CD11c⁺ cell→CD3⁺ T cell interactions (Fig. 2g). NSAIDs function by inhibiting the synthesis of pro-inflammatory signaling molecules and chemo-attractants derived from arachidonic acid¹⁸, including eicosanoids such as prostaglandins and leukotrienes. Notably, reduced CD11c⁺ cell→CD3⁺ T cell interactions were observed for sulindic sulfoxide, salicin, celecoxib, tomelukast and zafirlukast, thus reaching the same phenotype across diverse modes of NSAID action ($P < 3.8 \times 10^{-5}$; Supplementary Fig. 3g)¹⁸. This suggested a strong sensitivity of the CD11c⁺ cell→CD3⁺ T cell interaction to modulation by NSAIDs, consistent with previous reports¹⁹.

Furthermore, several drugs altered leukocyte cell-cell interactions with known mechanisms of action that were not directly linked to the previously described steroidal, NSAID or nervous-system-related mode of action. Quinine compounds strongly reduced CD11c⁺ cell→CD3⁺ T cell interactions (Fig. 2g,h), consistent with their anti-inflammatory effect and interference in MHC presentation, which has led to their current clinical use in the management of rheumatoid arthritis and other inflammatory diseases²⁰. Cholesterol-lowering drugs also reduced CD11c⁺ cell→CD3⁺ T cell interactions (Fig. 2g), which possibly could have been mediated by the well-documented dependency of MHC-II antigen presentation on cholesterol-enriched lipid rafts^{21,22}. A subset of cholesterol-lowering drugs, the HMG-CoA reductase inhibitors (statins), which also reduced CD11c⁺ cell→CD3⁺ T cell interactions (Fig. 2g and Supplementary Fig. 3h), have been reported to also function in a cholesterol-independent way via blocking of leukocyte function-associated antigen (LFA)-1-mediated adhesion to and co-stimulation of lymphocytes²³. Incubation with angiotensin-converting enzyme (ACE) inhibitors, particularly enalapril and its active metabolite enalaprilat, led to increased CD14⁺ cell clustering, as well as increased CD14⁺ cell↔CD19⁺ B cell interactions (Fig. 2g and Supplementary Fig. 3h), which potentially could be related to their reported inhibitory effect on the expression of the chemokine CCL2 (also known as MCP1)²⁴, which inhibits B cell migration²⁵. Taxifolins and catechols included plant flavonoids with known antioxidant and anti-inflammatory activity²⁶, which led to decreased CD14⁺ cell clustering (Fig. 2g,h). Furthermore, *N*-acyl-L-homoserine lactones (components of the bacterial quorum-sensing machinery) led to increased CD3⁺ T cell clustering and reduced CD19⁺ B cell→CD3⁺ T cell interactions (Fig. 2g), which have been shown to activate the immune system and increase survival in pretreated mice of a mouse model of bacterial infection²⁷, and a related compound has been shown to interfere with T cell differentiation²⁸, although the mechanism of their recognition and effect on T cells is as yet unresolved.

Finally, the screen revealed several neurological modulators, which mimic or interfere with signaling of the nervous system (particularly the sympathetic nervous system) that regulates a close physiological connection between the nervous and immune systems, as having immunomodulatory potential²⁹. For instance, modulators of the neurotransmitter γ -aminobutyric acid (GABA) signaling increased CD19⁺ B cell clustering (potentially indicating activation; Fig. 2g). GABA, which is expressed on most PBMC subpopulations³⁰, has been shown to have an anti-inflammatory role in mouse models of autoimmune disorders involving B cells, including multiple sclerosis³¹ and rheumatoid arthritis³², suggesting that it may be involved in B cell-mediated effects. In addition, agonists and antagonists of the β -adrenergic receptors altered several CD3⁺ T cell-centered cell-cell contacts (Fig. 2g), consistent with the reported expression and function of the β -adrenergic receptors on lymphocytes³³. β -adrenergic receptor agonists increased CD3⁺ T cell→CD11c⁺ cell interactions and decreased both CD3⁺ T cell clustering and CD3⁺ T cell→CD19⁺ B cell interactions, whereas β -adrenergic receptor antagonists enriched for decreased CD19⁺ B cell→CD3⁺ T cell interactions (Fig. 2g), which is likely related to the diverse effects of β 2-adrenergic receptor signaling on distinct subsets of T cells that have been reported previously³⁴.

Taken together, image-based screening of PBMCs enabled the exploration and categorization of the chemical rewiring of the leukocyte cell-cell interaction network, which revealed results consistent with a variety of previously reported studies, and all of these observations were made from a single phenotypic screen performed on the leukocytes of a single donor blood sample. The screen described here identified small compounds that can modulate and inhibit immune function, implicated novel modes of action for several compounds and existing drugs, and validated numerous effects through imaging.

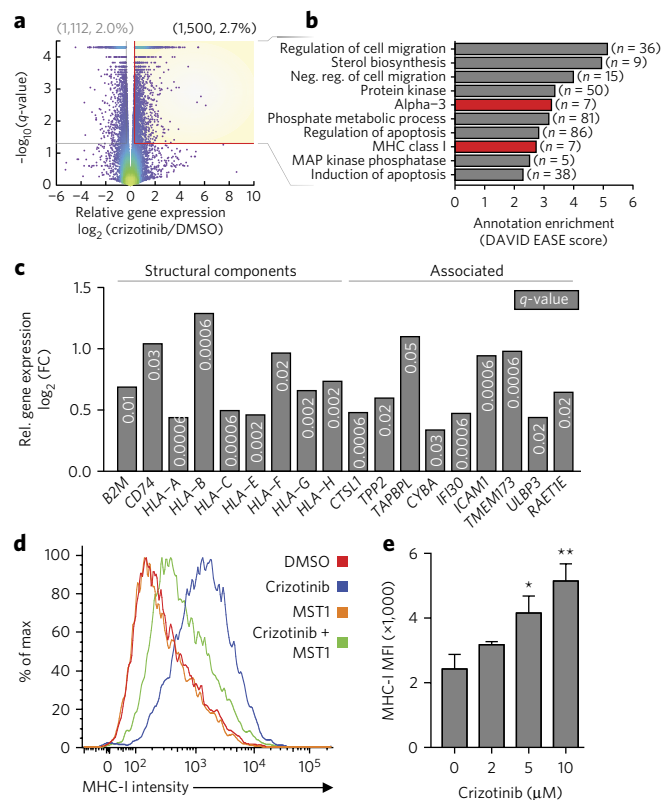


Figure 4 | Crizotinib drives MHC-I expression in SW480 colon cancer cells. (a,b) Significance (y axis) and log₂(fold change) (x axis) of gene expression (as determined by RNA-seq analysis) in SW480 cells after 72 h of 2 μ M (*R*)-crizotinib treatment relative to that in cells treated with DMSO (yellow box indicates genes that were significantly upregulated (by one-way analysis of variance (ANOVA)); $n = 1,500$ genes) (a) and annotation enrichment analysis of the genes that were significantly upregulated by crizotinib treatment (b). In a, dots indicate individual genes, and dot color indicates local data density. In b, selected top-enriched annotations are shown; MHC-related classes are indicated in red. (c) Relative gene expression (log₂(fold change); y axis) for selected genes from a,b. (d,e) Flow cytometry analysis for intensity (d) or mean fluorescence intensity (MFI) (e) of MHC-I expression on SW480 cells after incubation with 3 μ M crizotinib (blue), 1 μ g/ml MST1 (orange), 3 μ M crizotinib + 1 μ g/ml MST1 (green) or DMSO (red) (d) or with increasing concentrations of crizotinib (e), overnight. In a-c, RNA-seq was performed in technical triplicates. Data in d,e are representative of three (d) or four (e) experiments.

Crizotinib increases interactions between T cells and APCs

An example of drugs with previously unknown immunomodulatory properties are the inhibitors of the receptor protein tyrosine kinases (RTKs), the use of which led to increased interactions between CD11c⁺ cells and CD3⁺ T cells (Figs. 2g and 3a), despite the fact that RTKs have rarely been shown to have immunomodulatory effects^{35,36}. The observed enrichment resulted from the strong phenotypes obtained for both enantiomers of the RTKi crizotinib (Fig. 3b). (*R*)-Crizotinib (hereafter referred to as crizotinib) is an inhibitor of the MET, ALK and ROS1 kinases³⁷ that has been approved for the treatment of ALK-rearranged non-small-cell lung carcinoma (NSCLC) and is under investigation for the treatment of several additional solid tumors.

We repeated the leukocyte interaction screen using the entire drug library and a blood sample from a second healthy donor, without background cell stimulation by VSV infection, and found that we could reproduce the specific crizotinib effect, namely that the RTKi drug class was the strongest-enriched drug class over all cell-cell

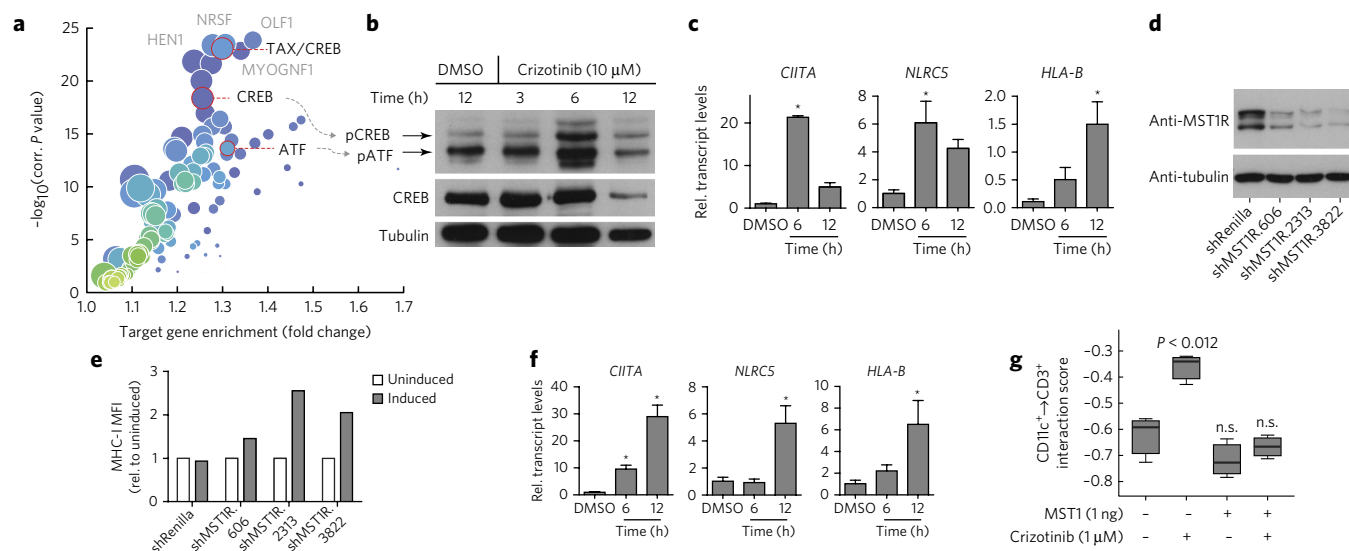


Figure 5 | Immunomodulatory effect of crizotinib is mediated by MST1R inhibition. (a) Analysis for transcription-factor-binding site enrichment in genes that were upregulated in **Figure 4a**. Filled circles correspond to annotations, circle sizes scale with the number of genes present in the annotation, and colors indicate local data density. (b) Representative western blot analysis for the phosphorylated and total level of the transcription factor CREB, and for the level of phosphorylated ATF, after incubation of SW480 cells with crizotinib. Tubulin was used as a loading control. (c) qPCR analysis for the expression of the indicated genes (relative to expression of the housekeeping gene *GAPDH*) after incubation with 10 μM crizotinib. Data are mean \pm s.e.m. (d) Representative western blot analysis for MST1R levels in lysates from SW4870 cells in which expression of the indicated siRNA was induced. (e) MFI of MHC-I expression after overnight induction of the indicated siRNAs. (f) qPCR analysis for the expression of the indicated genes (relative to *GAPDH* expression) after incubation with 1 μM BMS-777607. Data are mean \pm s.e.m. (g) Interaction scores of CD11c⁺ \rightarrow CD3⁺ cells after overnight incubation of human PBMCs from a healthy donor with crizotinib and/or MST1. In box-and whisker plots, boxes denote 25th to 75th percentiles, and whiskers indicate the maximal data points present within 1.5 \times IQR from the top and bottom of the boxes of technical repeat values. In **b-g**, data are representative of three (**b,d,e,g**) or four (**c,f**) experiments. In **c,f,g**, *P* values were determined by a *t*-test; **P* < 0.05.

interactions (**Fig. 3c**), with a significant increase in the number of interactions between CD11c⁺ cells and lymphocytes (i.e., monocyte-marker-negative cells) observed after crizotinib treatment (**Supplementary Fig. 4a**). Because MHC-to-TCR contact-dependent signaling drives APC \rightarrow T cell interactions and downstream activation, we assayed for altered MHC expression after crizotinib treatment of PBMCs from additional healthy donors, using flow cytometry, and observed a dose-dependent increase of surface-expressed MHC-II levels on CD11c⁺ cells that was not observed in cells that were treated with an unrelated cytotoxic compound (digitoxin) or with DMSO (**Fig. 3d**). Furthermore, addition of an MHC-II-specific blocking antibody strongly decreased the crizotinib-enhanced interaction between CD11c⁺ monocytes and CD3⁺ T cells, indicating that MHC-II upregulation mediated the observed immunomodulatory effect (**Fig. 3e**). Comparison of the T cell compartment after *ex vivo* crizotinib incubation of PBMCs indicated that there was a crizotinib-induced CD4⁺ T helper 1 (T_H1), but not T_H2, response, which is indicative of an inflammatory and cytotoxic immune milieu (**Fig. 3f** and **Supplementary Fig. 4b**).

Expression of genes encoding MHC-I and MHC-II molecules is partially under the control of overlapping transcription factors³⁸, and MHC-I's ability to present self-antigens is a crucial factor in mounting a successful anticancer immune response³, in which increased MHC-I expression and antigen presentation on cancer cells is a desirable effect in the treatment and maintenance of cancer³⁹. We therefore measured the transcriptional response using RNA sequencing (RNA-seq) analysis in the colorectal-adenocarcinoma-derived cell line (SW480 cells) after treatment with 2 μM crizotinib (**Fig. 4a** and **Supplementary Data Set 3**). The genes upregulated by crizotinib treatment showed significant enrichment for MHC-I annotations (**Fig. 4b,c**), including those encoding all three major MHC-I cell

surface receptors (*HLA-A*, *HLA-B* and *HLA-C*), the invariant chain β 2-microglobulin (*B2M*) (**Fig. 4c**) and factors involved in antigen presentation, as well as peptide processing, loading and trafficking (**Fig. 4c**). Although MHC-II expression is typically restricted to professional APCs, the gene encoding the invariant chain of MHC-II (*CD74*) was also significantly upregulated on SW480 cells after crizotinib treatment (**Fig. 4c**). Crizotinib-enhanced expression of MHC-I on the SW480 cell surface was confirmed by flow cytometry (**Fig. 4d,e**).

Analysis for the enrichment of transcription-factor-binding sites in the upregulated genes revealed a strong enrichment of binding sites for CREB and ATF (**Fig. 5a**), both of which are important transcription factors for the expression of MHC-I and MHC-II class molecules; these transcription factors further regulate and cooperate with the MHC-class-specific transcription factors *CIITA* and *NLRC5* (refs. 38,40). Indeed, we observed increased phosphorylation of both CREB and ATF after crizotinib treatment of SW480 cells (**Fig. 5b** and **Supplementary Fig. 5a**), as well as increased levels of the *CIITA* and *NLRC5* transcripts (**Fig. 5c**).

We recently identified the spectrum of targets for crizotinib in SW480 cells, using chemical proteomics⁴¹, and among the most abundant interactors in these cells was the macrophage-stimulating 1 receptor (MST1R; also known as RON), a close MET homolog. Crizotinib has been described to have a dissociation constant of 25 nM to MST1R⁴² and to inhibit MST1R with a half-maximal inhibitory concentration (IC₅₀) of approximately 200 nM⁴³, and KINOMEScan results have shown 100% binding of MST1R at 1 μM (*R*)-crizotinib⁴¹. MST1R is a known negative regulator of MHC-II expression and immune function in mice, as activation by its ligand, MST1, leads to decreased phosphorylation of the transcription factor STAT1 and decreased *CIITA* expression^{44,45}. Furthermore, because naive *MST1R*-knockout mice show increased immune cell

infiltration in lungs⁴⁶, we thus speculated that crizotinib treatment could increase MHC expression by inhibition of MST1R.

We used inducible short hairpin RNAs (shRNA) to target *MST1R* expression in SW480 cells and found that the loss of *MST1R* function coincided with increased cell surface expression of MHC-I molecules after 72 h of efficient *MST1R* knockdown (Fig. 5d,e and Supplementary Fig. 5b–d), whereas no such increase was observed for the negative control shRNA (Fig. 5e). Furthermore, treatment of SW480 cells with a more potent and specific *MST1R* inhibitor, BMS-777607 (ref. 47), also led to strong upregulation of *CIITA*, *NLRC5* and *HLA-B* expression (Fig. 5f), whereas, as expected, treatment with the ligand *MST1* did not induce expression of these genes (Supplementary Fig. 5e). Increased cell surface expression of MHC-I after treatment with BMS-777607 was confirmed by flow cytometry (Supplementary Fig. 5f), whereas incubation with *MST1* showed no change in cell surface expression of MHC-I (Fig. 4d and Supplementary Fig. 5f). Notably, combined incubation of SW480 cells with *MST1* and crizotinib led to reduced cell surface expression of MHC-I to levels comparable to those seen with crizotinib treatment alone (Fig. 4d), and further competition experiments using crizotinib and *MST1* in blood from a healthy donor revealed a full reversal of the crizotinib-increased interactions between CD3⁺ T cells and CD11c⁺ monocytes (Fig. 5g).

To test whether crizotinib also induced MHC-I expression *in vivo*, we injected crizotinib or vehicle alone into immunodeficient SCID mice that harbored a SW480 xenografted tumor. Using immunohistochemistry, we found that tumors from the crizotinib-treated mice had significantly higher levels of MHC-I expression than tumors from the vehicle-treated control mice (Fig. 6a,b), which recapitulated the *ex vivo* immunomodulatory effect of crizotinib *in vivo*.

The immunomodulatory effect of crizotinib was not limited to blood from healthy individuals or the SW480 colon carcinoma cell line; analysis of publicly available transcriptomics data of an ALK-positive NSCLC-derived cell line that was made resistant to crizotinib by prolonged incremental exposure to the drug (up to 1 μ M) also revealed increased expression of MHC-I- and MHC-II-encoding genes relative to that observed for the crizotinib-sensitive parental H3122 cell line⁴⁸ (Supplementary Fig. 6a–c). We confirmed this by qPCR, measuring strong upregulation of transcript abundance of *CIITA*, *NLRC5* and *HLA-A* after crizotinib treatment of the parental H3122 cells (Supplementary Fig. 6d). Furthermore, we performed chemical proteomics with the racemic mixture of crizotinib in H3122 cells, which revealed extensive binding of *MST1R* also in this setting (Supplementary Table 2). Thus, crizotinib interacted with *MST1R* and led to increased expression of MHC-molecule-encoding genes also in this cell line model for NSCLC, a disease for which crizotinib is clinically approved. Of note, *MST1R* may be a relevant crizotinib target in NSCLC, as a meta-analysis of 15 studies measuring gene expression in lung cancers showed consistent and significant upregulation of *MST1R* specific to NSCLC (Supplementary Fig. 6e).

The presentation of self-antigens on MHC-I by cancer cells is a key step in the anticancer immune response of the host and is essential for several checkpoint inhibitor treatments that are currently under investigation³⁹. To test the immunomodulatory potential of crizotinib in primary patient-derived material, PBMCs from a patient diagnosed with chronic myelomonocytic leukemia who had greater than 70% CD33⁺ and CD34⁺ blast cells in peripheral blood were incubated *ex vivo* with crizotinib. Crizotinib-treated peripheral blasts showed a twofold increase in cell surface expression of MHC-I as measured by flow cytometry (Fig. 6c), as well as a concentration-dependent increase in T cell \leftrightarrow blast interactions as measured by automated microscopy (Fig. 6d). The anticancer effects of genetic ablation and chemical inhibition of *MST1R* have been shown *in vivo* in mouse models of lung cancer and have revealed increased CD8⁺ T cell infiltration of tumors, resulting

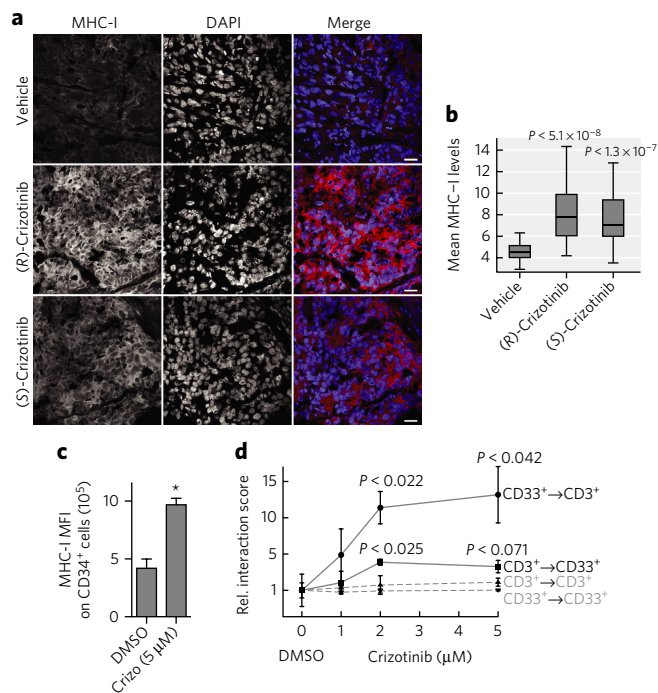


Figure 6 | *In vivo* assessment of the immunomodulatory potential of crizotinib. (a,b) Immunohistochemistry imaging of SW480 xenograft tumors stained with an antibody specific for human MHC-I (a) and quantification of MHC-I expression levels ($n = 3$ tumors per group, and $n = 8$ images per tumor; 40 \times images; scale bars, 20 μ m) (b) after treatment with vehicle or with 50 mg per kg body weight (mg/kg) (R)-crizotinib or (S)-crizotinib. In box-and-whisker plots, boxes denote 25th to 75th percentiles, and whiskers indicate the maximal data points present within 1.5 \times IQR from the top and bottom of the boxes of technical repeat values. (c,d) MFI of MHC-I expression on CD34⁺ blasts (c) and DMSO-relative interaction scores between CD33⁺ blasts and CD3⁺ T cells (d) after crizotinib treatment in PBMCs from a patient who was diagnosed with acute myeloid leukemia (AML) after previously having had chronic myelomonocytic leukemia (CMML). In c,d, experiments were performed in triplicate and are representative of three repeats. In b-d, *P* values were calculated by a *t*-test; **P* < 0.05.

in reduced metastasis⁴⁵. Taken together, our data suggest that the crizotinib-mediated *MST1R* inhibition and the subsequent increase in cell surface levels of MHC-I on colon, lung and blood cancer cells may aid an anticancer immune response and be beneficial for clinical use in combination with immunotherapy for a range of malignancies (Supplementary Fig. 6f)⁸. A clinical trial that combines treatment with crizotinib and CTLA-4 blockade by ipilimumab for the treatment of NSCLC (NCT01998126) may reveal whether clinical anticancer immune responses benefit from the immunomodulatory effect of crizotinib we describe here.

DISCUSSION

Here we define the possibility to systematically quantify and identify the immunomodulatory potential of drugs and biologicals in the complex multilineage populations in PBMCs of one individual. Prior to this, the technical options and models for measuring system-wide immunomodulatory events in a high-throughput manner were limited, which drove the need for such a screening tool. The data set provides evidence for the immunomodulatory potential of ~150 chemical agents, many of which have not been reported to display effects on the immune system and may thus become the objects of further investigation. Similarly to that of crizotinib, it is conceivable that the immunomodulatory potential of some of these agents

unknowingly contributes to the clinical success of individual drugs. Although the library here was screened at a single concentration for each drug, it is feasible that additional effects may become apparent at higher, but still safe, concentrations. This large-scale functional characterization of the current collection of ‘common’ drugs represents a new dimension and a potential future standard assay in the characterization of existing and new drugs. It remains to be seen how often the effects reported here result in altered cell-cell interactions, cell infiltrations and altered immune functions in other tissues. Certainly, the platform can easily be adapted to screen for new agents that aim at specific immunomodulatory effects. Equally exciting is the perspective to perform ‘personalized’ assessments on individual patients or healthy donors on a routine basis. The systematic perturbation of the immune system of an individual over such a varied array of pathways and processes may thus provide a unique functional ‘profile’ of the health status of a person, which is likely to depend on age, gender, diet, and transient and chronic infections. We illustrated how the approach could be useful in identifying agents that function in an immunomodulatory manner in cancer; however, other diseases characterized by increased inflammation, such as rheumatoid arthritis or autoimmune diseases, may be particularly interesting to consider for future studies. The finding that crizotinib, a drug in clinical use, may exert some of its antitumor activity through an immunomodulatory effect not only helps define the full mechanism of action, but it also may broaden crizotinib’s therapeutic use to other indications. In general, the modulation of the immune system by small compounds may be a desirable integrated positive effect that is more common than previously expected and that may be a result of their full polypharmacological properties^{49,50}.

Received 21 September 2016; accepted 17 January 2017;
published online 24 April 2017

METHODS

Methods, including statements of data availability and any associated accession codes and references, are available in the [online version of the paper](#).

References

- Snijder, B. *et al.* Population context determines cell-to-cell variability in endocytosis and virus infection. *Nature* **461**, 520–523 (2009).
- Germain, R.N., Robey, E.A. & Cahalan, M.D. A decade of imaging cellular motility and interaction dynamics in the immune system. *Science* **336**, 1676–1681 (2012).
- Mahoney, K.M., Rennert, P.D. & Freeman, G.J. Combination cancer immunotherapy and new immunomodulatory targets. *Nat. Rev. Drug Discov.* **14**, 561–584 (2015).
- Hoos, A. Development of immuno-oncology drugs—from CTLA4 to PD1 to the next generations. *Nat. Rev. Drug Discov.* **15**, 235–247 (2016).
- Sharma, P. & Allison, J.P. The future of immune checkpoint therapy. *Science* **348**, 56–61 (2015).
- Roche, P.A. & Furuta, K. The ins and outs of MHC class II-mediated antigen processing and presentation. *Nat. Rev. Immunol.* **15**, 203–216 (2015).
- Hou, W. *et al.* Viral infection triggers rapid differentiation of human blood monocytes into dendritic cells. *Blood* **119**, 3128–3131 (2012).
- Germain, R.N. & Stefanová, I. The dynamics of T cell receptor signaling: complex orchestration and the key roles of tempo and cooperation. *Annu. Rev. Immunol.* **17**, 467–522 (1999).
- Wu, L.C., Tuot, D.S., Lyons, D.S., Garcia, K.C. & Davis, M.M. Two-step binding mechanism for T cell receptor recognition of peptide–MHC. *Nature* **418**, 552–556 (2002).
- Banchereau, J. & Steinman, R.M. Dendritic cells and the control of immunity. *Nature* **392**, 245–252 (1998).
- Lolekha, S., Dray, S. & Gotoff, S.P. Macrophage aggregation *in vitro*: a correlate of delayed hypersensitivity. *J. Immunol.* **104**, 296–304 (1970).
- Maloney, D.G., Smith, B. & Rose, A. Rituximab: mechanism of action and resistance. *Semin. Oncol.* **29**, 2–9 (2002).
- Löffler, A. *et al.* Efficient elimination of chronic lymphocytic leukemia B cells by autologous T cells with a bispecific anti-CD19–anti-CD3 single-chain antibody construct. *Leukemia* **17**, 900–909 (2003).
- Topp, M.S. *et al.* Safety and activity of blinatumomab for adult patients with relapsed or refractory B precursor acute lymphoblastic leukemia: a multicenter, single-arm, phase 2 study. *Lancet Oncol.* **16**, 57–66 (2015).
- Honke, N. *et al.* Enforced viral replication activates adaptive immunity and is essential for the control of a cytopathic virus. *Nat. Immunol.* **13**, 51–57 (2011).
- Hu, X., Li, W.P., Meng, C. & Ivashkiv, L.B. Inhibition of IFN- γ signaling by glucocorticoids. *J. Immunol.* **170**, 4833–4839 (2003).
- Glass, C.K. & Saijo, K. Nuclear receptor *trans*-repression pathways that regulate inflammation in macrophages and T cells. *Nat. Rev. Immunol.* **10**, 365–376 (2010).
- Dennis, E.A. & Norris, P.C. Eicosanoid storm in infection and inflammation. *Nat. Rev. Immunol.* **15**, 511–523 (2015).
- Harizi, H., Corcuff, J.B. & Gualde, N. Arachidonic-acid-derived eicosanoids: roles in biology and immunopathology. *Trends Mol. Med.* **14**, 461–469 (2008).
- Ben-Zvi, I., Kivity, S., Langevitz, P. & Shoenfeld, Y. Hydroxychloroquine: from malaria to autoimmunity. *Clin. Rev. Allergy Immunol.* **42**, 145–153 (2012).
- Anderson, H.A., Hiltbold, E.M. & Roche, P.A. Concentration of MHC class II molecules in lipid rafts facilitates antigen presentation. *Nat. Immunol.* **1**, 156–162 (2000).
- Komaniwa, S. *et al.* Lipid-mediated presentation of MHC class II molecules thymocytes to the CD4 lineage. *Eur. J. Immunol.* **39**, 96–112 (2009).
- Weitz-Schmidt, G. *et al.* Statins selectively inhibit leukocyte function antigen 1 by binding to a novel regulatory integrin site. *Nat. Med.* **7**, 687–692 (2001).
- Schindler, R., Dinarello, C.A. & Koch, K.M. Angiotensin-converting-enzyme inhibitors suppress synthesis of tumor necrosis factor and interleukin 1 by human peripheral blood mononuclear cells. *Cytokine* **7**, 526–533 (1995).
- Flaishon, L. *et al.* Expression of the chemokine receptor CCR2 on immature B cells negatively regulates their cytoskeletal rearrangement and migration. *Blood* **104**, 933–941 (2004).
- Rice-Evans, C.A., Miller, N.J., Bolwell, P.G., Bramley, P.M. & Pridham, J.B. The relative antioxidant activities of plant-derived polyphenolic flavonoids. *Free Radic. Res.* **22**, 375–383 (1995).
- Khajanchi, B.K., Kirtley, M.L., Brackman, S.M. & Chopra, A.K. Immunomodulatory and protective roles of quorum-sensing signaling molecules *N*-acyl homoserine lactones during infection of mice with *Aeromonas hydrophila*. *Infect. Immun.* **79**, 2646–2657 (2011).
- Ritchie, A.J. *et al.* The *Pseudomonas aeruginosa* quorum-sensing molecule *N*-3-(oxododecanoyl)-l-homoserine lactone inhibits T cell differentiation and cytokine production by a mechanism involving an early step in T cell activation. *Infect. Immun.* **73**, 1648–1655 (2005).
- Elenkov, I.J., Wilder, R.L., Chrousos, G.P. & Vizi, E.S. The sympathetic nerve—an integrative interface between two supersystems: the brain and the immune system. *Pharmacol. Rev.* **52**, 595–638 (2000).
- Alam, S., Laughton, D.L., Walding, A. & Wolstenholme, A.J. Human peripheral blood mononuclear cells express GABAA receptor subunits. *Mol. Immunol.* **43**, 1432–1442 (2006).
- Bhat, R. *et al.* Inhibitory role for GABA in autoimmune inflammation. *Proc. Natl. Acad. Sci. USA* **107**, 2580–2585 (2010).
- Tian, J., Yong, J., Dang, H. & Kaufman, D.L. Oral GABA treatment downregulates inflammatory responses in a mouse model of rheumatoid arthritis. *Autoimmunity* **44**, 465–470 (2011).
- Sanders, V.M. The β 2-adrenergic receptor on T and B lymphocytes: do we understand it yet? *Brain Behav. Immun.* **26**, 195–200 (2012).
- Loza, M.J., Foster, S., Peters, S.P. & Penn, R.B. β -agonists modulate T cell functions via direct actions on type 1 and type 2 cells. *Blood* **107**, 2052–2060 (2006).
- Heine, A., Held, S.A., Bringmann, A., Holderried, T.A. & Brossart, P. Immunomodulatory effects of anti-angiogenic drugs. *Leukemia* **25**, 899–905 (2011).
- Santoni, M. *et al.* Role of natural and adaptive immunity in renal cell carcinoma response to VEGFR-TKIs and mTOR inhibitor. *Int. J. Cancer* **134**, 2772–2777 (2014).
- Cui, J.J. *et al.* Structure-based drug design of crizotinib (PF-02341066), a potent and selective dual inhibitor of mesenchymal-epithelial transition factor (c-MET) kinase and anaplastic lymphoma kinase (ALK). *J. Med. Chem.* **54**, 6342–6363 (2011).
- Kobayashi, K.S. & van den Elsen, P.J. NLR5: a key regulator of MHC class I-dependent immune responses. *Nat. Rev. Immunol.* **12**, 813–820 (2012).
- Sharma, P. & Allison, J.P. Immune checkpoint targeting in cancer therapy: toward combination strategies with curative potential. *Cell* **161**, 205–214 (2015).
- Moreno, C.S., Beresford, G.W., Louis-Pence, P., Morris, A.C. & Boss, J.M. CREB regulates MHC class II expression in a CIITA-dependent manner. *Immunity* **10**, 143–151 (1999).
- Huber, K.V.M. *et al.* Stereospecific targeting of MTH1 by (S)-crizotinib as an anticancer strategy. *Nature* **508**, 222–227 (2014).

42. Davis, M.I. *et al.* Comprehensive analysis of kinase inhibitor selectivity. *Nat. Biotechnol.* **29**, 1046–1051 (2011).
43. Christensen, J.G. *et al.* Cytoreductive antitumor activity of PF-2341066, a novel inhibitor of anaplastic lymphoma kinase and c-Met, in experimental models of anaplastic large-cell lymphoma. *Mol. Cancer Ther.* **6**, 3314–3322 (2007).
44. Wilson, C.B. *et al.* The RON receptor tyrosine kinase regulates IFN- γ production and responses in innate immunity. *J. Immunol.* **181**, 2303–2310 (2008).
45. Eyob, H. *et al.* Inhibition of Ron kinase blocks conversion of micrometastases to overt metastases by boosting antitumor immunity. *Cancer Discov.* **3**, 751–760 (2013).
46. Mallakin, A. *et al.* Gene expression profiles of Mst1r-deficient mice during nickel-induced acute lung injury. *Am. J. Respir. Cell Mol. Biol.* **34**, 15–27 (2006).
47. Schroeder, G.M. *et al.* Discovery of *N*-(4-(2-amino-3-chloropyridin-4-yloxy)-3-fluorophenyl)-4-ethoxy-1-(4-fluorophenyl)-2-oxo-1,2-dihydropyridine-3-carboxamide (BMS-777607), a selective and orally efficacious inhibitor of the Met kinase superfamily. *J. Med. Chem.* **52**, 1251–1254 (2009).
48. Lovly, C.M. *et al.* Rationale for co-targeting IGF-1R and ALK in ALK-fusion-positive lung cancer. *Nat. Med.* **20**, 1027–1034 (2014).
49. Knight, Z.A., Lin, H. & Shokat, K.M. Targeting the cancer kinome through polypharmacology. *Nat. Rev. Cancer* **10**, 130–137 (2010).
50. Zhang, J., Yang, P.L. & Gray, N.S. Targeting cancer with small-molecule kinase inhibitors. *Nat. Rev. Cancer* **9**, 28–39 (2009).

Acknowledgments

We are grateful to the donors and patients for their part in this study. Our screening compound libraries are from the US National Institutes of Health clinical collection or as gifts from F. Bracher, T. Nielsen, S. Nijman, J. Bradner, the Broad Institute and Haplogen GmbH. JQ1 was provided by S. Knapp (University of Oxford), and H3122 cells

and SW480 cells were kind gifts from E. Haura (Moffitt Cancer Center) and W. Berger (Medical University of Vienna), respectively. We thank M. Rebsamen, A. Fauster, G. Jurisic, A. César-Razquin, C.C. West, E. Girardi and G. Winter for assistance and critical reading of the manuscript and members of G.S.-F's laboratory for scientific discussions. CeMM is supported by the Austrian Academy of Sciences. We acknowledge funding from an ERC i-FIVE Advanced Investigator Grant (G.S.-F.), Austrian Science Fund grant F4711-B20 (G.S.-F.), the Austrian Federal Ministry of Science, Research and Economy (S.K.), the National Foundation for Research, Technology and Development (S.K.), the Swedish Cancer Society (T.H.), the Knut and Alice Wallenberg Foundation (T.H.), the Torsten and Ragnar Söderberg Foundation (T.H.), Swiss National Science Foundation Fellowships (P300P3_147897 (B.S.), PP00P3_163961 (B.S.) and P2EZP3_159114 (N.K.)), an EMBO long-term Fellowship (1543-2012; G.I.V.) and a Marie-Sklodowska Curie Action Fellowship (SLIM; N.K.).

Author contributions

G.I.V., B.S., N.K., J.W.B., K.V.M.H., C.-H.L., K.S., A.R., U.W.B. and M.S. performed the experiments; P.K. and U.J. organized the clinical samples; S.K. and O.L.d.l.F. provided reagents and intellectual contributions; P.K., U.J., T.H. and G.S.-F. were responsible for human and animal ethical guidelines; G.S.-F. oversaw the project; and B.S., G.I.V. and G.S.-F. analyzed the data and wrote the manuscript.

Competing financial interests

The authors declare competing financial interests: details accompany the [online version of the paper](#).

Additional information

Any supplementary information, chemical compound information and source data are available in the [online version of the paper](#). Reprints and permissions information is available online at <http://www.nature.com/reprints/index.html>. Publisher's note: Springer Nature remains neutral with regard to jurisdictional claims in published maps and institutional affiliations. Correspondence and requests for materials should be addressed to G.S.-F.

ONLINE METHODS

Collection and purification of peripheral blood and bone marrow cells. Peripheral blood was obtained from healthy donors, from patients with CMML who were treated at the Medical University of Vienna/General Hospital Vienna and from the Austrian Red Cross. The Austrian Red Cross provided plasma and red blood cell (RBC)-depleted enriched buffy coats from healthy donors. Blood coagulation was prevented by the addition of EDTA or heparin. The Ethics Commission at the Medical University of Vienna—General Hospital Vienna approved the collection of samples from healthy donors and patients. All donors and patients provided written informed consent after the nature and consequences of the study were explained. All donors were blind to the end users. Peripheral blood was diluted 1:1–1:3 in PBS, and mononuclear cells were isolated with a lymphoprep density gradient from Axis-Shield according to the manufacturer's instructions. Purified cells were suspended in RPMI medium (Gibco) supplemented with 10% FBS and penicillin-streptomycin. For all experiments involving primary cells, cells were cultured in RPMI medium supplemented with 10% FBS and penicillin-streptomycin.

Non-adherent PBMC monolayer formation, small-molecule screening, viruses, reagents and cell lines. 50 nl of selected screening compounds in DMSO, and DMSO controls, were transferred to Corning 384-well, tissue-culture-treated clear-bottom plates by a Labcyte Echo liquid handler attached to a PerkinElmer high-content cell:explorer workstation. Screening-compound libraries were obtained from the NIH Molecular Libraries Program or as gifts from various groups (see Acknowledgments), or they were designed in-house. Selected compounds routinely underwent quality control by mass spectrometry. The compounds screened are outlined in **Supplementary Data Set 1**. 50 μ l of culture medium containing approximately 40×10^4 cells/ml was pipetted into each well of a 384-well plate and incubated at 37 °C with 5% CO₂; cells were allowed to settle to the bottom. For virus screens, cells were incubated with compound for 3 h before VSV that expressed GFP was added (in 10 μ l) at a multiplicity of infection (MOI) = 10 for 18 h. The screen in **Figure 2** was performed in quadruplicate (global level) and duplicate (population level) using 384-well plates, and blood from a single healthy donor; see figure legends for technical replicate information for other experiments. For the healthy donor spatial screen without VSV expressing GFP, PBMCs were incubated with compound for 36 h. For blocking antibody experiments, anti-human-HLA-DR (G46-6; 3 μ g/ml) (eBiosciences), anti-human-CD54 (HA58; 3 μ g/ml) (BD Biosciences) or mouse-IgG2a isotype control (Cl.18.4; 1:300) (BioXCell) was incubated for 3 h before overnight stimulation with VSV or with 10 ng/ml LPS (Invivogen). HLA-DR-specific blocking antibody was incubated overnight before treatment with crizotinib for 3 h. The indicated concentrations of rituximab (anti-human-CD20; Absolute Antibody) or blinatumomab (Amgen, Vienna General Hospital in-patient pharmacy) was incubated with healthy donor blood overnight or for 48 h, respectively. Recombinant MST1 was from R&D Systems. All screens were stopped by fixing and permeabilizing the cells with 10 μ l of a solution of 4% formaldehyde and 0.01% Triton-X114 in PBS for 10 min at room temperature. Fixative-containing medium was removed, and 30 μ l of an experiment-dependent antibody cocktail in PBS was added to the cells for 1 h at room temperature; all antibodies (listed next) were used at a 1:300 dilution. Antibodies were selected for their ability to identify specific populations of interest: anti-human-CD19 (HIB19; allophycocyanin-conjugated); for B cells), anti-CD11c (3.9; allophycocyanin-conjugated; for the majority of dendritic cells and monocytes), anti-CD3 (HIT3a; phycoerythrin (PE)-conjugated; for T cells), anti-CD14 (61D3; PE-conjugated; for macrophages and monocytes) and anti-CD34 (4H11; allophycocyanin-conjugated; for hematopoietic progenitors) from eBiosciences, anti-CD20 (2H7, fluorescein-conjugated; for B cells) from BD Biosciences and anti-CD56 (A07788, PE-conjugated; for NK cells) from Beckman Coulter were all used in various combinations to identify populations of interests in each experiment, as described in the text. DAPI (at 10 μ M; Sigma) was used for the detection of nuclei. SW480 and H3122 cells were cultured in Dulbecco's modified Eagle's medium (DMEM) or RPMI medium, respectively, that was supplemented with 10% FBS and penicillin-streptomycin. H3122 cells were a gift from Eric Haura (Moffitt Cancer Center), and SW480 cells were a gift from Walter Berger (Medical University of Vienna). The cells used in

the experiments were routinely tested for mycoplasma contamination by enzyme-linked immunosorbent assay (ELISA) and PCR.

Flow cytometry. PBMCs or SW480 cells were either kept unstimulated or incubated with small-molecule compounds for the indicated amounts of time. In addition to the antibodies used for imaging, anti-human-HLA-DQ (SK10, fluorescein isothiocyanate (FITC)-conjugated; for the MHC-II⁺ population), anti-HLA-ABC (G46-2.6, PE- and cyanine 5 (Cy5)-conjugated; for the MHC-I⁺ population), anti-CD4 (SK3, PE-conjugated; for the T cell subset), anti-CD183 (CXCR3-173; FITC-conjugated; for the T cell subset) and anti-CD194 (CCR4-D8SEE; allophycocyanin-conjugated; for the T cell subset) from eBiosciences were used for flow cytometry. Samples were run on a BD LSRFortessa instrument with Diva software and analyzed with FlowJo.

Western blots. SW480 cells were plated overnight and stimulated at the indicated time points. Pellets were lysed using IP lysis buffer (50 mM Tris-HCl (pH 7.5), 150 mM NaCl, 5 mM EDTA, 1% Nonidet P-40, 50 mM NaF, 1 mM Na₃VO₄, 1 mM PMSF and 5 g/ml tosyl phenylalanyl chloromethyl ketone (TPCK)) and a protease inhibitor mixture for 10 min on ice before high-speed clearance, and the protein content of the lysate was quantified using the Bradford (Bio-Rad) assay. Proteins were detected with rabbit anti-phospho-CREB(Ser113) (87G3; 1:1,000), mouse anti-CREB (86B10; 1:1,000) or rabbit anti-RON (C81H9; 1:1,000) (all from Cell Signaling), and mouse anti-tubulin (Abcam; 1:5,000), which were visualized using a goat anti-mouse or anti-rabbit (H + L) horseradish peroxidase (HRP)-conjugated secondary antibody (Jackson ImmunoResearch Laboratories; 1:10,000) and exposed on film.

RNA isolation and quantitative PCR (qPCR). RNA was purified from SW480 or H3122 cells using an RNeasy Kit (Qiagen) and was reverse-transcribed using oligo-dT primers and the RevertAid Reverse Transcriptase (Fermentas). qPCR was performed using SensiMix SYBR Green (Bioline) analyzed on a Rotor-Gene Q from Qiagen. Gene expression for *CIITA* (Forward (F): GGCTGGAATTTGGCAGCAC, Reverse (R): GCCCAACAC AAGGATGTCTC), *NLR5* (F: CTGGCCAGTCTACCCGCACAA, R: CCA GGGACAGCCATCAAAATC), *HLA-A* (F: AAAAGGAGGGAGTTACACT CAGG, R: GCTGTGAGGGACACATCAGAG), and *HLA-B* (F: CTCATGGTC AGAGATGGGGT, R: TCCGCAGATACCTGGAGAAC) were normalized to that of the housekeeping gene *GAPDH* (F: GAAGGTGAAGTCCGGAGT, R: GAAGATGGTGTATGGGATTTC).

Inducible knockdown of *MST1R* expression. 97-mer shRNA sequences were obtained as ultramer oligonucleotides (Integrated DNA Technologies; IDT), PCR-amplified and cloned into the inducible retroviral microRNA (miR)-E shRNA vector pRT3GEN (pSIN-TRE3G-turboGFP-miR-E-PGK-NeoR) as described previously using standard cloning techniques⁵¹. The Tet-on competent SW480 cells were generated by virally transducing the vector pMSCV-RIEP (pMSCV-rtTA3-IRES-EcoR-PGK-PuroR) and standard retroviral packaging. After virus infection, transformed cells were selected using 5 μ g/ml puromycin (Sigma-Aldrich), and SW480RIEP cells were transduced in a similar manner using the retroviral shRNA vector pRT3GEN. The following 97-mer target sequences were used: *Renilla* luciferase at position 713: GCTGTTGACAGTGAGCGCAG GAATTATAATGCTTATCTATAGTGAAGCCACAGATGTATAGATAA GCATTATAATTCCTATGCCTACTGCCTCGGA; *MST1R* at position 606: TG CTGTTGACAGTGAGCGATCCCGGTGACACAGACACAAATAGT GAAGCCACAGATGTATTTGTGTCTGTGCACCGGGAGTGCCTACTG CCTCGGA; *MST1R* at position 2,313: TGCTGTTGACAGTGAGCGACC AGTGCTGATAGCAGTGCAATAGTGAAGCCACAGATGTATTGCA CTGCTATCAGCACTGGCTGCCTACTGCCTCGGA; and *MST1R* at position 3,822: TGCTGTTGACAGTGAGCGAAGGGAGTACTATAGTGTTC AATAGTGAAGCCACAGATGTATTGAACACTATAGTACTCCCTGTGCCTAC TGCCTCGGA. Following virus transduction and selection using 2 mg/ml G418 (Roth), shRNA expression was induced by the addition of 2 μ g/ml doxycycline to the culture medium. MHC-I expression was analyzed by flow cytometry 72 h after doxycycline addition. pRT3GEN-sh*Ren.713*, which expresses an shRNA targeting the *Renilla* luciferase-encoding sequence served as negative control shRNA. The MFI of MHC-I expression (PE-Cy5 channel) was

normalized to that observed in the absence of doxycycline. Knockdown efficiency was determined by western blot analysis, as described above.

RNA sequencing (RNA-seq) analysis. SW480 cells were seeded in 6-well plates 24 h before (*R*)-crizotinib was added to a final concentration of 2 μ M. After incubation for 72 h, medium was aspirated, and cells were washed with PBS. Total RNA was isolated using the RNeasy kit (Qiagen), and RNA concentration was measured using the Qubit 2.0 Fluorometric Quantitation system (Life Technologies), using the manufacturers' protocols. RNA integrity number (RIN) was determined using Experion Automated Electrophoresis System (Bio-Rad). RNA-seq libraries were prepared with TruSeq Stranded mRNA LT Sample Preparation Kit (Illumina) using Sciclone and Zephyr liquid-handling robotics (PerkinElmer). Library concentration was quantified using the Qubit 2.0 Fluorometric Quantitation system (Life Technologies), and the size distribution was assessed using Experion Automated Electrophoresis System (Bio-Rad). Sequencing libraries were pooled, diluted and sequenced on an Illumina HiSeq 2000 instrument using 50-bp single-read chemistry. The base calls provided by the Illumina Realtime Analysis software were converted into a BAM format using Illumina2bam and demultiplexed using BamIndexDecoder (<https://github.com/wtsi-ngp/illumina2bam>). Transcriptome analysis was performed using the Tuxedo suite. TopHat2 (v2.0.10)⁵² was supplied with reads that passed vendor quality-filtering (PF reads) and with the Ensembl transcript set (Homo sapiens, e73, September 2013) as reference. TopHat2 analyses were run independently for each replicate. Cufflinks (v2.1.1)⁵³ was used to assemble transcripts from spliced read alignments, using both the Ensembl e73 transcriptome as reference, as well as *de novo* assembly of transcript models. Differential expression was assessed with Cuffdiff v2.1.1⁵⁴. Transcriptome sets of all replicates for each sample group were combined with Cuffmerge. Finally, cummeRbund (<http://www.bioconductor.org/packages/release/bioc/html/cummeRbund.html>) and biomaRt (<http://www.bioconductor.org/packages/release/bioc/html/biomaRt.html>) were used in combination with custom R scripts to perform quality assessment and further refine the analysis results. All sequencing was performed by the Biomedical Sequencing Facility at CeMM (<http://medical-epigenomics.org>). SW480 RNA sequencing results are available in **Supplementary Data Set 3** and at the NCBI Gene Expression Omnibus (GEO) database under accession code [GSE93124](https://www.ncbi.nlm.nih.gov/geo/query/acc.cgi?acc=GSE93124). Transcription data from ALK⁺ H3122 cells resistant to crizotinib treatment were obtained from those at GEO under accession code [GSE49508](https://www.ncbi.nlm.nih.gov/geo/query/acc.cgi?acc=GSE49508).

Drug-affinity chromatography and protein mass spectrometry. The crizotinib affinity probe was prepared in two steps from commercially available 3-[(1*R*S)-1-(2,6-dichloro-3-fluorophenyl)ethoxy]-5-[1-(piperidin-4-yl)-1H-pyrazol-4-yl]pyridin-2-amine (S1068, Selleckchem) according to the literature, and drug-affinity matrices were prepared as described previously⁴¹. Briefly, affinity chromatography and elution were performed in duplicate using 25 nmol of compound that was immobilized on 50 μ l NHS-activated Sepharose 4 Fast Flow beads (GE Healthcare Bio-Sciences) and 10 mg total cell lysate as protein input per replicate. For competition experiments, cell lysates were pretreated with 20 μ M 3-[(1*R*S)-1-(2,6-dichloro-3-fluorophenyl)ethoxy]-5-[1-(piperidin-4-yl)-1H-pyrazol-4-yl]pyridin-2-amine for 30 min. Eluates were labeled with iTRAQ (ABI), and quantitative protein mass spectrometry and bioinformatics analysis using the R isobar package were performed as previously reported^{48,55}.

Xenograft mouse model and immunohistochemistry. All mice were acclimatized for 1 week, and they had free access to water and food during the experiment. Mice were kept under a 12-h light cycle, and temperature, humidity and housing were kept per laboratory animal guidelines and regulations. The group size was based on previous experience of variability of tumor growth within control groups. Mice were grouped based on body weight; exclusion and inclusion criteria were pre-established in the ethical permit; and outliers in body weight were excluded, although no mice were excluded from this study based on the pre-established criteria. Groups were not randomized. Severe combined immunodeficient (SCID) mice (5- to 6-week-old female, Scanbur; $n = 3$ /group) were injected subcutaneously with 1×10^6 SW480 cells, together with a matrix gel (1:1), in the sacral area. Treatment was initiated 1 d after cell inoculation.

Vehicle, (*S*)-crizotinib or (*R*)-crizotinib was administered subcutaneously once daily at 25 mg/kg for 35 d. (*S*)-crizotinib or (*R*)-crizotinib was diluted in 1% DMSO, 10% ethanol, 10% cremaphore, 10% Tween 80 and 69% PBS. Mice were euthanized 2 h after the last administration of drugs on day 26. Tumors were quickly dissected, snap-frozen and kept at -80 °C until further analysis. Tumor sections were fixed in acetone for 10 min and rinsed in TBS. The sections were blocked in 3% BSA in TBS. An MHC-I-specific antibody (MHC class I clone W6/32; BioLegend; 1:250) was diluted in 3% BSA in TBS and incubated overnight at 4 °C in a humid atmosphere. After incubation, the slides were rinsed in TBS containing 0.025% Triton-X. An Alexa-Fluor-555-conjugated secondary antibody (Invitrogen) was diluted 1:500 in 3% BSA in TBS and added to the slides for 1 h at room temperature. The slides were counterstained with DAPI and mounted with Prolong Gold (Thermo Fisher Scientific). Images were taken on an LSM780 confocal microscope (Zeiss) with equal laser-line power settings over all of the samples. Eight random images were taken from three tumors per group; image analysis was performed by experimenters who were blinded to the identity of the samples. All experiments involving mice followed protocols approved by Stockholms Norra djurförsöksetiska nämnd (laboratory animal ethical committee Stockholm) and were in compliance with the 2010/63/EU directive.

Image and computational analysis. *Imaging.* Each well of a 384-well plate was imaged at 10 \times magnification with 2×2 non-overlapping images, so that approximately 95% of the well surface area was covered within the 2×2 square. The images were taken sequentially from the DAPI, GFP, PE and APC channels, with lasers and bandpass filter sets set so that the channels were non-overlapping; a PerkinElmer Operetta or Opera Phenix automated spinning-disk confocal microscope was used. Fluorophores were tested for channel separation on each machine. The raw .tiff images were exported from the microscope for analysis and stored for subsequent data mining.

Illumination correction. Illumination correction was performed based on a novel algorithm that depends on the observation that PBMCs in the monolayer never fully cover the entire well but that they always leave adequate space in between individual cells or clusters of cells to estimate regional background intensities. Because we imaged each well entirely (including regions of wells outside of the images), we first detected regions of each image that contained areas outside of the well, based on image reconstruction of the full well and plate-wide analysis of where areas outside of the wells were most likely to occur. For each individual single-channel image, a two-dimensional (2D) polynomial with two degrees of freedom in each dimension was fit on \log_{10} -transformed(1 + intensity) values, excluding regions of images containing areas outside of the well, excluding the brightest 30% of the signal (working under the assumption that a bright signal is not a background signal, which does not hold for bright-field images), and weighted to a combination of the inverse signal intensity (to weigh dark regions heavier) and a smooth function that weights edges of images heavier, as those are relatively underrepresented as compared to the typically brighter center of the image. Because the illumination correction function for each individual image is described in the efficient form of a polynomial function, goodness of fit statistics, and background patterns and intensities could be compared across each image from the same channel from the entire plate to detect outliers ($3 \times$ interquartile range (IQR) from median statistics). For outliers, fits were retried with different parameters (excluding larger regions of potential areas outside of wells); if that failed, then they were corrected with plate-average background correction functions for images of the same channel and at the same site within the other wells. The remaining outlier wells were flagged as having potential technical problems. The algorithm has been optimized for robustness over hundreds of imaged 384-well plates containing PBMCs, and improvements in separation of negatively, singly, and doubly stained cells have been confirmed.

Background correction. Image-based small-compound screens suffer from the fact that small compounds themselves can be sources of a fluorescence signal, which can overlap in unpredictable ways with the wavelengths of the imaged channels. To correct for small (within $3 \times$ IQR from median) background-intensity variations, which could also stem from other sources such as light source fluctuations, we further corrected for global background differences within all images of the same channel and of each well, and across

all wells of the same plate. Outlier background values per well were flagged as potentially auto-fluorescent-compound-containing or otherwise problematic wells and were discarded from the final screen statistics. Finally, illumination- and background-corrected images were reconstructed and stored independently for further image analysis. Improvements at the level of image quality and image analysis results were confirmed, and robustness of the algorithm was improved over hundreds of plates.

Image quality evaluation. All (illumination- and background-corrected) images of each plate were automatically rescaled and merged per well and per plate, allowing for quick visual evaluation of the quality over the entire data set of a single plate.

Single-cell image analysis using CellProfiler (code availability). Single-cell image analysis was performed using CellProfiler v2, based on DAPI-stain-derived nucleus ('Nuclei') detection, expansion from nucleus for cell outline detection ('Cells'), and a second and third set of expansions from Cells, to identify a ring outside of each cell for a local background ('LocalBackground') area sampling. Standard CellProfiler intensity, texture and shape features were measured from Nuclei, Cells and the LocalBackground over all channels where applicable. Differences between the log-transformed intensities of Nuclei and Cells relative to those for LocalBackground were used for the plate-wide identification of marker-positive cells in a supervised manner for the large-scale drug screens. Unsupervised thresholding was performed based on the predominant marker-negative cell population over the entire plate. Thresholds were regularly visually controlled at the plate-wide population distribution level, as well as at the single-cell level, relating images and image-analysis results.

Support vector machine (SVM)-based machine learning for quality control. Iterative SVM-based machine learning was applied at the level of individual cells to identify poorly segmented cells, cells covered by contaminants or artifacts ('blobs'), or cells identified as false positives, as described previously^{4,56}.

Plate-effect correction. Plate-effect correction was performed using a weighted 2D polynomial fit, excluding positive control wells and 5% of the strongest outlier wells, and weighted based on a function that weights outside wells stronger than inside wells, and outlier wells weaker than wells closer to the plate median. Globally, improvements in reproducibility across replicate wells that came from plates with individually randomized plate layouts, as well as in the separation of positive and negative control wells, were confirmed.

Statistical analysis. Significance calculation and hit selection for large-scale screens. For the large-scale screens, data sets were normalized for plate effects and normalized to the median of the DMSO controls of each plate; significance of the hits was calculated based on a Student's *t*-test of mean equals 0, over all replicated wells ($n = 4$ for the virus screens). Final infection and viability scores were calculated as the average over all replicates. Hits were selected based on $P < 0.01$ and on an absolute average *z*-score of at least 2. All other significance scores in the figures were calculated using a two-tailed *t*-test, unless otherwise noted.

Compound annotation enrichment analysis. Compounds were annotated based on their annotations as stored in the database and ontology of Chemical

Entities of Biological Interest (CHEBI) from the European Bioinformatics Institute (<http://www.ebi.ac.uk/chebi/>), as well as from the Kyoto Encyclopedia of Genes and Genomes (KEGG) Compound database (<http://www.genome.jp/kegg/compound/>). Overall, this retrieved 136 unique annotations for the compounds in our library. Enrichment scores were calculated as two-tailed *t*-tests between the phenotypes of compounds with a given annotation relative to the phenotypes of compounds without that given annotation.

Cell-cell interaction analysis. Pairwise distances (measured in pixels) between all cells in a well were calculated over a reconstruction of nuclear positions over the different images for each well. Cells were considered pairwise if the pairwise distance between nuclear centroids was 15 pixels. The observed fraction of A→B interacting cells equals the fraction of (all type A cells interacting with one or more type B cell). This fraction was log₂-transformed against the (E_{AB}) value calculated for that well, i.e., (the fraction of type A cells of all cells) × (the fraction of type B cells of all cells) × (the fraction of all cells that have at least one or more contacts within 15 pixels). Results were confirmed to be insensitive to reasonable increments of the '15-pixel' threshold. Although the reference value (E_{AB}) is independent of the direction of interaction, A→B and B→A can diverge as a consequence of the interaction conformation of the two subpopulations; for instance, so-called 'rosettas' that exist for a type A cell bound to many B cells can induce strongly divergent results between A→B and B→A. Readouts were corrected for plate effects, as described above, and analyzed further by various means, including drug class enrichment analyses and hit selection strategies, also as described above.

Data availability. The RNA-seq data from **Supplementary Data Set 3** can be found at GEO under accession code **GSE93124**). The protein interactions from this publication, listed in **Supplementary Table 1**, have been submitted to the IMEx (<http://www.imexconsortium.org>) Consortium through IntAct and have been assigned the identifier **IM-25603**. The data sets integrated for the meta-analysis of *MST1R* expression in lung cancers (**Supplementary Fig. 6e**) was retrieved from <http://www.oncomine.com> (exact data sets are referenced below the figure). The transcription data from ALK⁺ H3122 cells resistant to crizotinib treatment were previously published and obtained from GEO under accession code **GSE49508**.

51. Fellmann, C. *et al.* An optimized microRNA backbone for effective single-copy RNAi. *Cell Rep.* **5**, 1704–1713 (2013).
52. Kim, D. *et al.* TopHat2: accurate alignment of transcriptomes in the presence of insertions, deletions and gene fusions. *Genome Biol.* **14**, R36 (2013).
53. Trapnell, C. *et al.* Differential analysis of gene regulation at transcript resolution with RNA-seq. *Nat. Biotechnol.* **31**, 46–53 (2012).
54. Trapnell, C. *et al.* Transcript assembly and quantification by RNA-seq reveals unannotated transcripts and isoform switching during cell differentiation. *Nat. Biotechnol.* **28**, 511–515 (2010).
55. Winter, G.E. *et al.* Systems-pharmacology dissection of a drug synergy in imatinib-resistant CML. *Nat. Chem. Biol.* **8**, 905–912 (2012).
56. Rämö, P., Sacher, R., Snijder, B., Begemann, B. & Pelkmans, L. CellClassifier: supervised learning of cellular phenotypes. *Bioinformatics* **25**, 3028–3030 (2009).